Magnetospheric toroidal Alfvén wave harmonics and the field line distribution of mass density

Richard E. Denton,[1] Kazue Takahashi,[2] Roger R. Anderson,[3] and Martin P. Wuest[4,5]

Received 20 August 2003; revised 25 March 2004; accepted 8 April 2004; published 2 June 2004.

[1] Measurements of electric and magnetic field taken by instruments on the Combined Release and Radiation Effects Satellite (CRRES) spacecraft on 29 July 1991 reveal seven or eight toroidal Alfvén wave frequency bands. By using observations of the waves near the magnetic equator and the symmetry of the theoretical modes as a function of magnetic latitude, we can identify which theoretical Alfvén wave harmonic corresponds to a particular frequency band. This, along with the *L* shell frequency dependence, gives convincing evidence that we are in fact observing the toroidal Alfvén mode. Because the harmonics of the toroidal Alfvén wave have a different response to mass density at different points along a magnetic field line, the frequencies of these harmonics can be used to infer the distribution of mass density along the field line. While there is a significant uncertainty in the results due to the uncertainty in the observed frequencies, it is nevertheless true that both the solution based on the peak (mean) frequencies and the majority of solutions using a Monte Carlo simulation of the effects of uncertainty in frequency show the same result, that there is a local maximum in ρ within about 30° of the magnetic equator. A similar result is found for the wave event observed on 28 August 1990, a local maximum in ρ within about 15° of the magnetic equator. These results imply that heavy ions are preferentially concentrated at the magnetic equator. *INDEX TERMS:* 2768 Magnetospheric Physics: Plasmasphere; 2730 Magnetospheric Physics: Magnetosphere—inner; 2752 Magnetospheric Physics: MHD waves and instabilities; 2753 Magnetospheric Physics: Numerical modeling; 7819 Space Plasma Physics: Experimental and mathematical techniques; *KEYWORDS:* field line distribution of mass density, field line resonance mode, toroidal Alfven wave

Citation: Denton, R. E., K. Takahashi, R. R. Anderson, and M. P. Wuest (2004), Magnetospheric toroidal Alfvén wave harmonics and the field line distribution of mass density, *J. Geophys. Res.*, *109*, A06202, doi:10.1029/2003JA010201.

1. Introduction

[2] Magnetospheric mass density controls the time response of the magnetosphere to solar wind perturbations and is thus important for space weather. Toroidal Alfvén waves (with azimuthal velocity and magnetic perturbations), also known as the field line resonant mode, are commonly observed in the magnetosphere [*Anderson et al.*, 1990; *Lessard et al.*, 1999]. They can be detected on the ground [*Waters et al.*, 1996], thus making possible the remote sensing of magnetospheric mass density simultaneously at a number of locations [*Menk et al.*, 1999].

[3] Toroidal Alfvén frequencies have been used by a number of authors to infer magnetospheric mass density (see references by *Denton and Gallagher* [2000], *Menk et al.* [1999], and *Denton et al.* [2001], plus *Chi et al.* [2000a] published since these other references). Because the harmonics of the toroidal Alfvén wave have a different response to mass density at different points along a magnetic field line, the frequencies of these harmonics can be used to infer the distribution of mass density along the field line. To understand this, note that the fundamental mode has its largest perturbation in velocity at the magnetic equator, whereas at the same location the second harmonic has a node in the velocity perturbation (Figure 1). Assuming, for instance, that the mass density is constant along the field line, one can calculate the frequencies of the fundamental and second harmonic and calculate the ratio of those two frequencies. However, if the mass density is increased in the vicinity of the equator, the frequency of the fundamental mode will be reduced, the frequency of the second harmonic will not be greatly affected, and the ratio of the fundamental frequency to the second harmonic frequency will be less than it would if the density were constant along the field line. Thus this ratio yields information about the mass density at the equator compared to the mass density off the equator. If one knows more than two frequencies, it is possible to get even more information about the field line dependence.

[1]Department of Physics and Astronomy, Dartmouth College, Hanover, New Hampshire, USA.
[2]Applied Physics Laboratory, Johns Hopkins University, Laurel, Maryland, USA.
[3]Department of Physics and Astronomy, University of Iowa, Iowa City, Iowa, USA.
[4]Space Science Department, Southwest Research Institute, San Antonio, Texas, USA.
[5]Now at INFICON Limited, Balzers, Principality of Liechtenstein.

0148-0227/04/2003JA010201$09.00

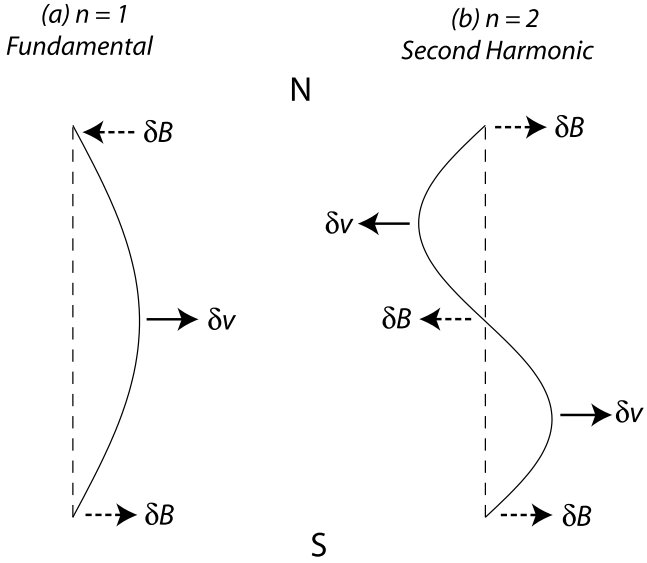

Figure 1. Sketch showing the symmetry of (a) symmetric modes like the fundamental $n = 1$ and (b) asymmetric modes like the second harmonic. For both modes, the dashed line is the unperturbed magnetic field line viewed from the equatorial plane, the north (south) ionospheric boundary is at the top (bottom), and the magnetic equator is at the middle. The perturbed field line is the solid curve, and the solid (dashed) arrows show the azimuthal perturbation in velocity $\delta\boldsymbol{\nu}$ (magnetic field $\delta\mathbf{B}$).

[4] Most attempts to infer the field line dependence have assumed a power law form for the mass density ρ

$$\rho = \rho_{eq}\left(\frac{R_{max}}{R}\right)^{\alpha}, \tag{1}$$

where ρ_{eq} is the equatorial mass density and R_{max} is the maximum distance to any point on the field line ($\sim LR_E$). *Takahashi and McPherron* [1982], *Engebretson et al.* [1986], and *Menk et al.* [1999] assumed equation (1) and used toroidal Alfvén harmonics to determine α ranging from 0 to 6, implying that ρ is a minimum at the magnetic equator. (However, as pointed out by *Denton and Gallagher* [2000], Takahashi and McPherron would have found a negative value for α in the case of one of their data points if their method had allowed for such a possibility.) *Price et al.* [1999] and *Denton et al.* [2001] used a more general method, which allowed for a nonmonotonic field line dependence.

[5] In order to use the toroidal Alfvén frequencies to determine ρ, the harmonic number associated with each frequency must be identified. Because of the symmetry of the modes about the magnetic equator (Figure 1), the latitudinal dependence of the perturbations can be used to help identify the modes [*Anderson et al.*, 1990; *Singer and Kivelson*, 1979]. *Singer et al.* [1979] observed the fundamental and second harmonic modes simultaneously on the same field line using electric and magnetic field measurements on the ISEE-1 spacecraft.

[6] The main uncertainty in determining the field line distribution of mass density from toroidal Alfvén frequencies results from the uncertainty of the frequencies themselves. While this calculation is straightforward if only a single frequency is measured (such as the fundamental mode), it is not so simple when the frequencies of multiple harmonics are measured. *Denton and Gallagher* [2000] first investigated the sensitivity of the equatorial mass density and power law coefficient α (equation (1)) to errors in multiple frequencies. *Denton et al.* [2001] used a polynomial expansion for mass density ρ as a function of position along the field line and determined the error in ρ using a Monte Carlo distribution of frequencies based on the widths of the spectral lines. They used a single time segment for the Fourier analysis in each event. In the case of the first event they studied (orbit 0081, 28 August 1990), it was possible to determine the frequencies accurately enough to show that there was a local peak in density at the magnetic equator. However, as will be shown later in this paper (Figures 2–4), the frequencies one measures will depend on the particular choice of the time segment. The danger of choosing a single time segment for the analysis is that the results may not be representative of the surrounding data. In fact, reexamination of the second event studied by Denton et al. (orbit 0920) has indicated that the power spectra used in that study were not stable enough to justify use of the fourth harmonic frequency (listed in that study) as the time window was shifted.

[7] In this paper, we determine the frequencies and their associated uncertainties more conservatively, by averaging the power spectra obtained over a number of time segments. We use electric and magnetic field measurements taken by the Combined Release and Radiation Effects Satellite (CRRES) on 29 July 1991 in order to identify eight toroidal Alfvén harmonics and use seven of these to infer the parallel distribution of mass density. We also reanalyze the 28 August 1990 event (orbit 0081) that was examined by *Denton et al.* [2001]. In sections 2 and 3, we describe the data and the method of computation, respectively. In section 4 we present our results for the 29 July 1991 event. Discussion follows in section 5, including a new analysis of the 28 August 1990 event.

2. Data

2.1. Instrumentation

[8] The CRRES spacecraft was launched in late July 1990 into an 18.2° inclination orbit with apogee at approximately geocentric distance (6.3 R_E) and perigee at an altitude of 350 km. The orbital period was about 10 hours. The satellite was spin stabilized, at a rate of 2 rpm, with its spin axis pointing within 15° of the Sun. The local time of apogee, initially at 0800, precessed toward the west at approximately 0.67° per day. In this study, we used data acquired by the fluxgate magnetometer [*Singer et al.*, 1992], the electric field experiment [*Wygant et al.*, 1992], the Plasma Wave Experiment (PWE) [*Anderson et al.*, 1992], and the Low-Energy Magnetospheric Ion Composition Sensor (LOMICS) [*Young et al.*, 1992]. High-resolution data is available from the magnetometer instrument, but we average the data to 15 s resolution, implying a Nyquist frequency of 33 mHz.

[9] The electric field experiments consisted of spherical and cylindrical sensors. We used data from the cylindrical

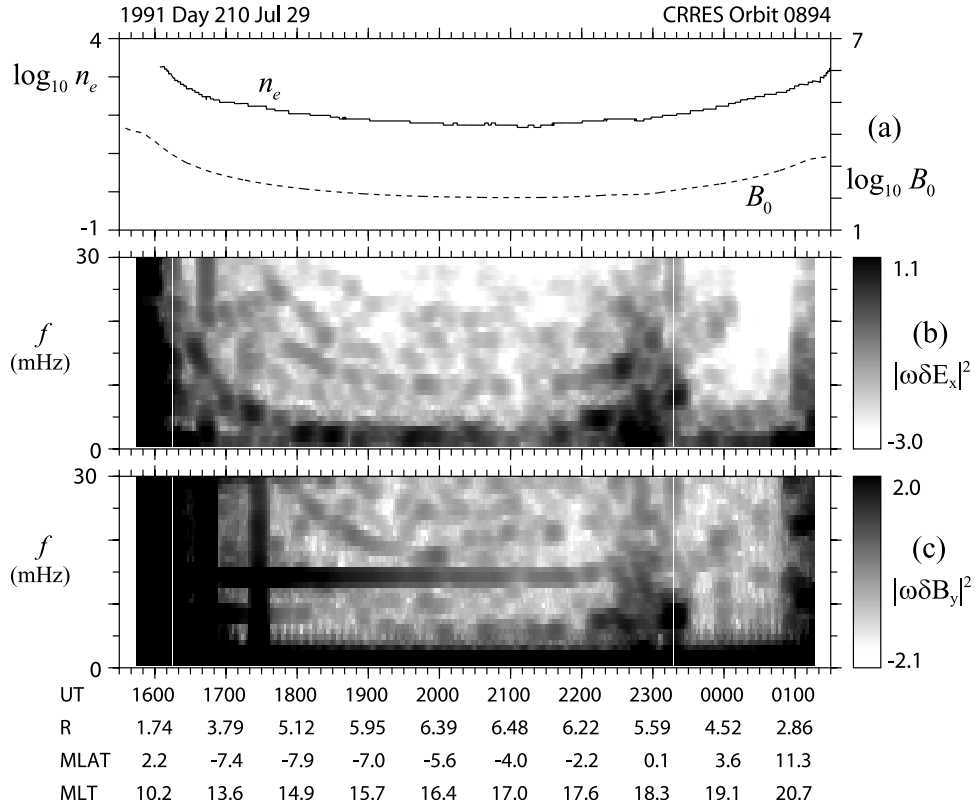

Figure 2. (a) The solid curve is the base 10 logarithm of the electron density N_e (in cm^{-3}), while the dashed curve is the logarithm of the ambient magnetic field B_0 (in nT). In Figures 2b and 2c the power spectra of the time derivative of the perturbations of the electric and magnetic field are plotted in grayscale, $|\omega\delta E_x|^2$ and $|\omega\delta B_y|^2$, respectively. The color bars at right in Figures 2b and 2c show the base 10 logarithm of the power spectral density in $(mV/(m\text{-}s))^2$ for $|\omega\delta E_x|^2$ (in Figure 2b) and in $(nT/s)^2$ for $|\omega\delta B_y|^2$ (in Figure 2c). At the bottom, R is in units of R_E, MLAT is in degrees, and MLT is in hours.

sensors. Data values are available at 15 s resolution, but the data values are averaged over the spacecraft spin period of approximately 30 s. This means that there is a 15 s overlap in the averaging period for adjacent data values. The net effect is that the electric field data will be of the highest quality up to 16.5 mHz, corresponding to the Nyquist frequency for 30 s resolution, but the electric field power spectrum will be gradually degraded as the frequency increases from 16.5 mHz to 33 mHz (corresponding to the Nyquist frequency for 15 s resolution). The electric field is sampled in the spacecraft spin plane. To get the electric field component along the spin axis (approximately the direction toward the Sun), it is assumed that there is no electric field $\boldsymbol{E}$ along the direction of the ambient magnetic field $\boldsymbol{B}_0$, that is, $\boldsymbol{E} \cdot \boldsymbol{B}_0 = 0$. This technique is considered to be reliable when the angle between the satellite spin plane and $\boldsymbol{B}_0$ is greater than 20° [*Maynard et al.*, 1996], which is the case for the data we will be using.

[10] Data from the Plasma Wave Experiment (PWE) are used to estimate the electron number density N_e from the upper hybrid noise band frequency [*Ledocq et al.*, 1994]. The log average and standard deviation are calculated over the period of time during which we examine the waves.

[11] Data from the Low-Energy Magnetospheric Ion Composition Sensor (LOMICS) was used to directly measure the mass density of ions with energy 60 eV and above [*Young et al.*, 1992]. Using these data, we find $\rho_{sc,obs}$, a lower limit for the mass density at the spacecraft location (Appendix A). Again, the log average and standard deviation are calculated during the period studied. The density values are listed in Table 1. As can be seen from Table 1, the additional mass density from ions with energy >60 eV did not significantly affect the mass density estimate. Therefore our mass density estimate is based mainly on data from the Plasma Wave Experiment. The LOMICS measurements certainly do not rule out the possibility that there could be a significant population of cold heavy ions with energies <60 eV.

2.2. Observations of Toroidal Alfvén Waves on 29 July 1991

[12] Figure 2 shows observations by CRRES on 29 July 1991. Spacecraft apogee (at $R \sim 6.5\ R_E$) occurs slightly after 2100 UT. Based on the dipole field model, the largest L value is reached at about 2040 UT (Figure 3d). These times are close to the times when minimum electron density N_e and ambient magnetic field B_0 (a 15 min boxcar log average of the magnitude of $\boldsymbol{B}_0$) are observed (Figure 2a). The spacecraft position averaged over the period 1930–2100 UT, along with Dst and Kp, is listed in Table 1.

[13] The fluctuating fields are calculated in a local field-aligned coordinate system. The $\hat{\boldsymbol{z}}$ direction is the direction of the ambient magnetic field, $\hat{\boldsymbol{y}} = -\hat{\boldsymbol{r}} \times \hat{\boldsymbol{z}}$, where $\hat{\boldsymbol{r}}$ is a unit vector in the radial direction, and $\hat{\boldsymbol{x}} = \hat{\boldsymbol{y}} \times \hat{\boldsymbol{z}}$. Thus $\hat{\boldsymbol{y}}$ roughly

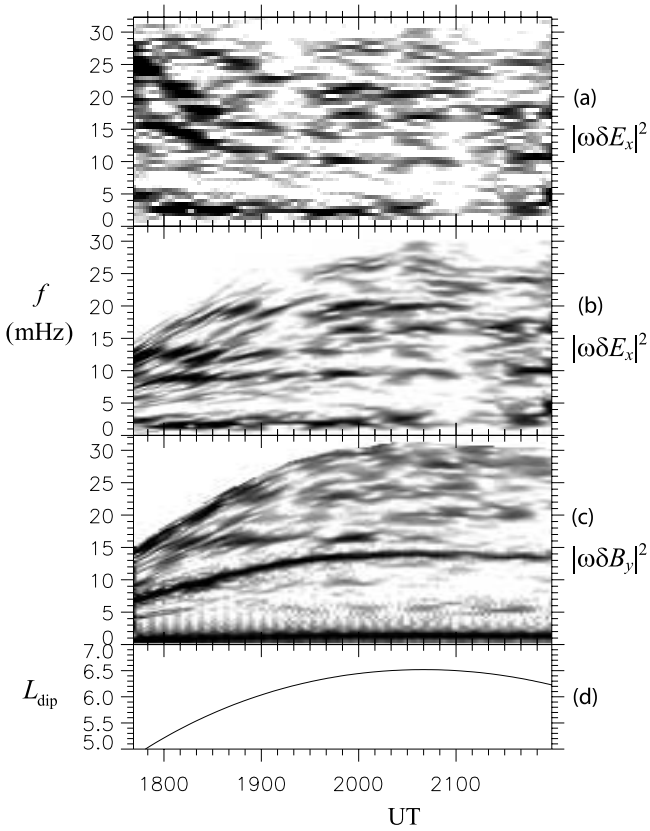

Figure 3. (a) Grayscale power spectrum of $|\omega\delta E_x|^2$ versus time as in Figure 2b. In Figure 3b the same quantity $|\omega\delta E_x|^2$ is plotted, but at each time, the frequency values have been normalized to $B_{0eq}/L_{dip}\sqrt{N_e}$ as described in the text. (c) Same as Figure 3b, except $|\omega\delta B_y|^2$ is plotted. (d) L_{dip} based on the dipole field model.

corresponds to the azimuthal direction, and $\hat{x}$ corresponds to a radial or L shell direction. In this paper, we will be studying the toroidal Alfvén wave, with velocity and magnetic field fluctuations in the $\hat{y}$ direction $\delta\nu_y$ and B_y, respectively (Figure 1). The associated electric field fluctuation is $\delta E_x \propto -\delta\nu_y B_0$.

[14] In Figure 2b and 2c, power spectra of $\omega\delta E_x$ and $\omega\delta B_y$, respectively, are shown. The power spectra are whitened (that is, the higher frequency spectrum is enhanced) by multiplying the Fourier coefficients by the frequency. In Figure 2c, the horizontal dark bands at 14 mHz and 0–3 mHz are due to noise associated with incorrect despinning of the data. Neglecting these, note the power in bands of emission that have a minimum in frequency at about 2100 UT (where L is a minimum) and shift to higher frequency at earlier and later times. For instance, in the $\omega\delta E_x$ power spectrum, there is a clear band with minimum frequency of about 10 mHz. These bands are due to toroidal Alfvén harmonics, as we will show.

[15] Figure 3a shows the same data as was plotted in Figure 2b, but the data analysis is slightly modified. The Fourier transforms are calculated in 30 min sliding time windows (at each time, a 30 min window is used to calculate the power spectrum), but the plotted time resolution is higher. Again, a number of emission bands are evident.

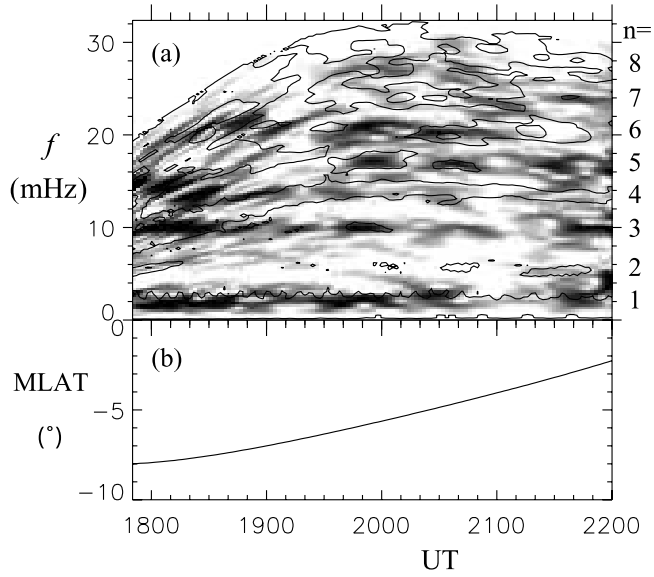

Figure 4. (a) Superimposed power spectra of $|\omega\delta E_x|^2$ (grayscale) and $|\omega\delta B_y|^2$ (contour line), and (b) SM coordinate system magnetic latitude MLAT.

[16] We expect the frequency of an Alfvén wave to be a number of order unity times a characteristic Alfvén speed divided by the length of the field line [*Denton and Gallagher*, 2000]. The simplest relevant Alfvén speed would be calculated at the magnetic equator (where B_0 is low, and therefore also the Alfvén speed V_A; this region has a dominant effect on the determination of the wave frequency f, since $1/f \approx \int ds/V_A$, where ds is the differential length along the field line). The length of the field line scales like L. Therefore we expect the frequency of the toroidal Alfvén wave to scale like $F_t \equiv B_{0eq}/(L\sqrt{N_e})$, where B_{0eq} is the local ambient magnetic

Table 1. Parameters for the Wave Events

Parameter	Event 1	Event 2
CRRES orbit	0894	0081
Date	29 July 1991	28 August 1990
Day of year	210	240
UT	1930–2100	0640–0810
R, R_E	6.40	6.23
MLAT, deg	−5.2	17.8
MLT, hours	16.6	6.77
Dst, nT	0.3	−22.7
p_{sw}, nPa		0.9
$B_{y\text{-}sw}$, nT		−1.2
$B_{z\text{-}sw}$, nT		5.5
Kp	1.0	1.7
B field model	T89	T96
R_{max}, R_E	6.44	7.24
$B_{sc,obs}$, nT	114.	148.
$B_{sc,Tsyg}$, nT	109.	136.
$N_{e\text{-}sc,obs}$, cm^{-3}	59.1 ± 4.6	13.3 ± 0.4
$\rho_{sc,LOMICS}$, amu cm^{-3}	0.9 ± 0.1	0.5 ± 0.1
$\rho_{sc,obs}$, amu cm^{-3}	60.1 ± 4.6	13.8 ± 0.4
$f_{obs\text{-}1}$, mHz	1.98 ± 0.45	2.56 ± 0.20
$f_{obs\text{-}2}$, mHz	5.77 ± 0.49	6.97 ± 0.31
$f_{obs\text{-}3}$, mHz	10.05 ± 0.28	10.72 ± 0.49
$f_{obs\text{-}4}$, mHz	13.72 ± 0.56	15.00 ± 0.50
$f_{obs\text{-}5}$, mHz	17.26 ± 0.34	19.07 ± 0.42
$f_{obs\text{-}6}$, mHz	20.56 ± 0.55	22.73 ± 0.45
$f_{obs\text{-}7}$, mHz	24.55 ± 0.72	26.20 ± 0.63

field mapped to the magnetic equator using the dipole field model, L is the L shell based on the dipole field model, and N_e is the local electron density based on the PWE measurements. (Here the density is assumed not to vary greatly between the spacecraft location and the magnetic equator.) The variable F_t is then implicitly a function of time t through the time dependence of the other variables.

[17] Figure 3b shows the same data as was plotted in Figure 3a, except that at each time, the frequencies have been multiplied by F_{2015}/F_t, where F_{2015} is evaluated at 2015 UT, close to the minimum in Alfvén frequency (Figure 3a). The effect is to level out the Alfvén frequency; that is, the Alfvén frequency at each time is similar to that which occurs at 2015 UT. In fact, the bands of wave power in Figure 3a that we associated with the toroidal Alfvén wave now appear to be roughly horizontal in Figure 3b showing that the frequency scales as we expect. This is clear evidence that these wave bands are in fact due to the toroidal Alfvén wave.

[18] The transformation in frequency leading to Figure 3b is also applied to the power spectrum of the magnetic field fluctuations in Figure 3c. The intense band of emission which has a frequency of 13.5 mHz at 2200 UT (right side of plot) increasing up to about 14 mHz at 2000 UT and then decreasing to about 7 mHz at 1750 UT (left side of plot) corresponds to the noise band which was at about 14 mHz in Figure 2c. Some toroidal wave emission can be observed just under this noise band between 2000 and 2100 UT indicating that there is a real wave band at about this frequency.

[19] In Figure 4a, the electric and magnetic field power spectra (with frequency transformation) are superimposed. The electric field power spectrum is plotted in grayscale, while one contour level is used to indicate the magnetic field power spectrum. Again, we need to be careful to recognize the noise bands for the magnetic field power spectrum; at the right side of the plot, one of these is at about 13 mHz, and one of these is below 3 mHz. Concentrating on the right side of the plot between 2100 and 2200 UT (for which MLAT is close to zero), we see an alternation in polarization in the bands of emission. At 2–4 mHz, there is a dark band indicating a fluctuation in electric field; the value $n = 1$ to the right of the plot marks this band. At about 5 mHz, we see contour lines indicating a fluctuation in the magnetic field; the value $n = 2$ to the right of the plot marks this band. At about 10 mHz, we see another dark band indicating a fluctuation in the electric field ($n = 3$). This alternating pattern continues along the right side of the plot, and n values up to 8 corresponding to these are listed to the right of the plot. In the case of the band at about 14 mHz, there is some uncertainty due to the noise band at that frequency, but it can be seen from Figure 3d that there is some wave power at around that frequency, at least between 1940 and 2200 UT.

[20] To see the alternation in polarization more clearly, we plot in Figure 5 an average from 2100 to 2200 UT of the power spectra plotted in Figure 3. That is, we average the power spectra computed for all time windows centered on times between 2100 and 2200 UT. Hence the widths of the spectral lines include the variation one gets due to different choices of the time window. The power spectrum of the electric field fluctuations (times frequency) is indicated by the dashed curve, while that of the magnetic fluctuations is indicated by the solid curve. The peaks marked by crosses are noise. A clear alternation in polarization can be seen in the peaks that are labeled $n = 1$ to 8 (with the exception of the magnetic field power spectrum for $n = 4$, which is obscured by noise; though see Figure 3c). The time period 2100–2200 UT corresponds to small but nonzero MLAT = −4 to −2° (Figure 4b). If the magnetic field were simply a dipole field, the magnetic equator would be at MLAT = 0°, but using the Tsyganenko 1989 magnetic field model [*Tsyganenko*, 1989], we find that the minimum value of B_0 (a better indication of the true magnetic equator) occurs at MLAT = −2°. (With the T96 magnetic field [*Tsyganenko*, 1995], assuming monthly average values for the solar wind parameters, we find a minimum at MLAT = −1°.) At any rate, the modes with odd n have a significant electric field or velocity perturbation near the magnetic equator, while the modes with even n have a significant magnetic perturbation there. The straightforward interpretation is that the bands with odd n correspond to symmetric modes, while the bands with even n correspond to asymmetric modes (see Figure 1). Seeing as it is the lowest frequency mode, it has the largest power (in the power spectrum of the electric field not multiplied by frequency) and has the right polarization (Figure 1a). We identify the $n = 1$ mode as the fundamental; $n = 2$ then corresponds to the second harmonic, and the higher values of n correspond to higher harmonics.

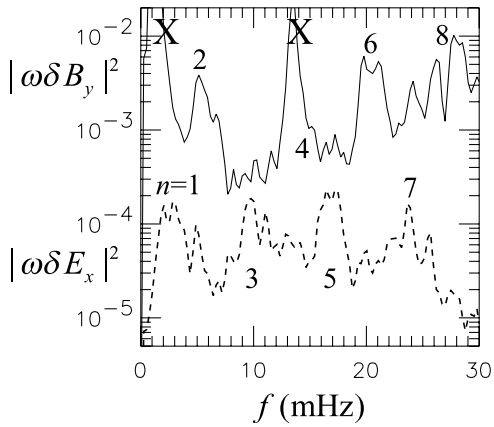

Figure 5. Log average of power spectra of $|\omega\delta E_x|^2$ in (mV/(m-s))^2 (dashed curve) and $|\omega\delta B_y|^2$ in (nT/s)^2 (solid curve) averaged between 2100 and 2200 UT. The large peaks marked by crosses are spurious noise.

[21] While the time period 2100–2200 UT is useful for examining the polarization, the frequencies of the modes are better defined in an earlier time period. Figure 6 shows the power spectra averaged over 1930–2100 UT in the same format as Figure 5. In this case, data such as that in Figure 3 was used for the averages, but with a 45 min average used for the power spectra. (Increasing the time window to 45 min decreased the width of the spectral peaks in Figure 6, but increasing the time window further did not result in any further improvement.) We can identify peaks corresponding to $n = 1, 3, 4, 5$, and 6 in the electric field, and $n = 2, 3, 5, 6$, and 7 in the magnetic field. We calculate the average frequency and standard deviation in each peak numerically; these are listed for $n = 1$–7 in Table 1. We will not use $n = 8$, since there

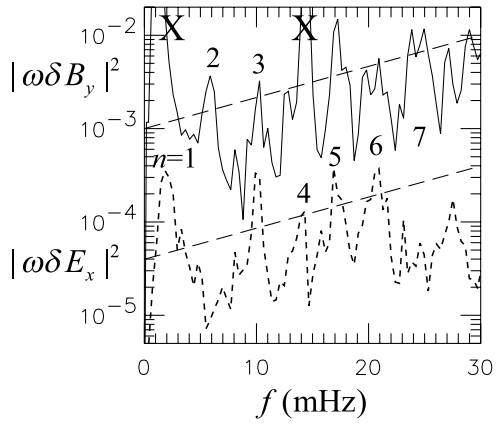

Figure 6. Same as Figure 5, but the averages are taken from 1930 to 2100 UT.

is some uncertainty as to the exact peak location in Figures 5 and 6. Further details on the calculation of the uncertainty in the observed frequencies is given in Appendix B; the dashed lines in Figure 6 will be described in paragraph 34.

3. Method of Calculation

[22] Given the frequencies of the toroidal Alfvén harmonics, we can solve for the mass density distribution along the field line. In brief, we assume some functional form for the mass density distribution along the field line and make a guess for the coefficients describing the distribution. We then solve the wave equation of *Singer et al.* [1981] to get the theoretical frequencies consistent with the mass density. We vary the coefficients of the mass density distribution until the theoretical frequencies match the observed ones. For any particular solution, we can also find as part of the solution the linear electric and magnetic field perturbations of each harmonic.

[23] For the most part, we use the method of *Denton et al.* [2001]; the discussion below touches on some important features of the analysis, stressing mainly the differences from their approach. The functional form for the mass density along the field line is either the power law form in equation (1) or a polynomial expansion for the base 10 logarithm of the mass density

$$\log_{10}\rho = c_0 + c_2\tau^2 + c_4\tau^4 + \ldots \tag{2}$$

in terms of the Alfvén crossing time coordinate τ, where

$$\tau \equiv \int \frac{ds}{V_A} \tag{3}$$

and the integral is calculated from the magnetic equator (position of minimum B_0) to any position along the field line. The quantity τ is then modified by multiplying by a linear function of the unadjusted τ so that $\tau = \pm 1$ at the two ionospheric boundaries (the linear term is only a slight adjustment and does not appear to significantly affect the results). The coordinate τ is the most natural choice for evaluating the mass density, since in the WKB approximation, the nodes of an Alfvén wave are evenly spaced with respect to this coordinate. Because the coordinate τ is itself a function of the field line distribution for ρ being sought, we use an iterative scheme so that the values of τ used in the final solution are consistent with the values of ρ.

[24] For this paper, we limit the solution to even powers of τ (as in equation (2)); that is, the field line distribution is assumed to be symmetric about the magnetic equator. We have done computations using odd powers, but the resulting solutions for ρ are not very well constrained. Small differences in the degree of agreement between observed and theoretical frequencies correspond to large differences in the field line distribution. Thus for this paper, we will circumvent this problem by assuming that the field line distribution is symmetric.

[25] *Denton et al.* [2001] used a nonlinear root solver to adjust the coefficients of the mass density distribution so as to match the theoretical and observed frequencies. Because of this, they were limited to use a number of observed frequencies equal to the number of coefficients describing the mass density distribution (so that the number of unknown quantities was equal to number of known quantities). For the results presented in this paper, we always use as input to the solution the total number of observed frequencies $f_{\text{obs-}n}$ listed in Table 1 (=7). When the number of coefficients is less than the number of observed frequencies, we minimize

$$\sigma_f \equiv \left(\frac{1}{N}\right)\sqrt{\sum_{n-1}^{N}\left(\frac{f_{\text{th}-n}}{f_{\text{obs}-n}} - 1\right)^2}, \tag{4}$$

where the theoretical and observed frequencies are $f_{\text{th-}n}$ and $f_{\text{obs-}n}$, respectively, and $N = 7$ is the number of frequencies. Further details on the method are given in Appendix C.

4. Solutions for Mass Density and Fields

4.1. Field Line Distribution of ρ From Frequencies

[26] We now solve for the mass density distribution along the field line by adjusting the coefficients of the mass density distribution so that the deviation between the theoretical and observed frequencies σ_f defined in equation (4) is minimized. Based on the peak frequencies for the 29 July 1991 event listed in Table 1, and using the power law density function in equation (1), we find $\rho_{\text{eq},\alpha\text{-peaks}} = 148$ amu/cm^3 and $\alpha_{\text{peaks}} = -5.5$, indicating that there is a peak in mass density at the magnetic equator. (These values are listed in Table 2. We use the subscripts "eq" or "sc" to indicate the density at the magnetic equator or spacecraft location, "obs," "α," or "poly" to indicate the observed quantity or a solution using the power law density in equation (1) or polynomial form in equation (2), and "peaks" or "ensem" to indicate a theoretical solution based on the peak frequencies or using an ensemble of frequencies as described in the next paragraph.)

[27] In order to estimate the uncertainty in the mass density distribution due to the uncertainty in the observed frequencies, we use a Monte Carlo simulation, calculating the mass density for an ensemble of frequency sets [*Denton et al.*, 2001]. More specifically, we generate 50 sets of the seven frequencies such that the standard deviation of the 50 values for each theoretical frequency $f_{\text{th-}n}$ is equal to the uncertainty of the observed frequency listed in Table 1. Averaging the fits from the ensemble of solutions, we find

Table 2. Observed and Computed Densities for Wave Events

Parameter	Event 1	Event 2
CRRES Orbit	0894	0081
Date	29 July 1991	28 August 1990
$\rho_{sc,obs}$, amu cm^{-3}	60.1 ± 4.6	13.8 ± 0.4
$\rho_{eq,\alpha\text{-peaks}}$, amu cm^{-3}	148.	33.
α_{peaks}	−5.5	0.1
$\rho_{sc,\alpha\text{-peaks}}$, amu cm^{-3}	143.	33.
$\rho_{eq,\alpha\text{-ensem}}$, amu cm^{-3}	127. ×÷ 1.5 (or 84–194)	33. ×÷ 1.3 (or 26–41)
α_{ensem}	−4.7 ± 5.4	−0.1 ± 1.8
$\rho_{sc,\alpha\text{-ensem}}$, amu cm^{-3}	124. ×÷ 1.5 (or 84–183)	32. ×÷ 1.1 (or 30–34)
$c_{0,peaks}$, $c_{0,ensem}$	2.1, 2.2 ± 0.4	1.6 1.6 ± 0.1
$c_{2,peaks}$, $c_{2,ensem}$	0.8, 1.3 ± 1.4	−0.6 −0.9 ± 0.3
$c_{4,peaks}$, $c_{4,ensem}$	−3.0, −4.9 ± 2.6	0.4 1.4 ± 4.2
$c_{6,peaks}$, $c_{6,ensem}$	1.5, 3.1 ± 2.1	0.4 −0.2 ± 3.6
$\rho_{sc,poly\text{-}peaks}$, amu cm^{-3}	137.	28.
$\rho_{sc,poly\text{-}ensem}$, amu cm^{-3}	128. ×÷ 1.9(68–244)	27. ×÷ 1.2 (22–32)

$\rho_{eq,\alpha\text{-ensem}} = 127$ ×/÷ 1.5 amu/cm^3 and $\alpha_{ensem} = -4.7 \pm 5.4$ (" ×/÷" indicates a multiplicative error resulting from the log average, $\log_{10} \rho_{eq,\alpha\text{-ensem}} = 2.11 \pm 0.18$, where $\rho_{eq,\alpha\text{-ensem}}$ is measured in amu/cm^3). This indicates that most solutions consistent with the uncertainties in frequency lead to a peak in mass density at the equator (negative α). A flat solution ($\alpha = 0$) is (just barely) within the uncertainty, but $\alpha = 3$ or 4, as is sometimes expected for a collisionless particle distribution [*Goldstein et al.*, 2001], is unlikely. The average MLAT value for the period of waves, 1930–2100 UT (during which we have calculated the average observed mass density $\rho_{sc,obs} = 60.1 \pm 4.6$ amu/cm^3), was MLAT = −5.2° (Figure 4b). For each solution in the ensemble, we calculate the mass density at this latitude, and after computing a log average find $\rho_{eq,\alpha\text{-ensem}} = 124$ ×/÷ 1.5 amu/cm^3. The lower end of this range, 124/1.5 = 84 amu/cm^3, is still larger than the observed mass density $\rho_{sc,obs} = 60.1 \pm 4.6$ amu/cm^3, indicating that there may be cold heavy ions present.

[28] In Figure 7, the results of our calculations are shown as a function of magnetic latitude MLAT and geocentric radius R. The bold curve is the solution based on the peak frequencies (equation (1) with $\rho_{eq,\alpha\text{-peaks}}$ and α_{peaks}). The three thin curves show the results of the Monte Carlo simulation; they are the logarithmic average and the logarithmic average plus or minus one standard deviation calculated at each position from the ensemble of solutions. (Because the plot has a log scale, the logarithmic average is vertically halfway between the upper and lower thin curves at each value of MLAT or R.) The mass density observed at the spacecraft location, $\rho_{sc,obs} = 60.1 \pm 4.6$ amu/cm^3, is plotted as an asterisk with error bars. Again, it is clear that the solution for ρ based on the peak frequencies and the majority of solutions from the Monte Carlo simulation have a local peak in mass density at the magnetic equator.

[29] Since we have seven frequencies, it is possible to use a functional form for mass density with more than two parameters. Figure 8 shows the results of our calculations using the polynomial form for mass density in equation (2). In this case, only c_0, c_2, c_4, and c_6 are nonzero. For other choices of polynomial coefficients, see Appendix D. As in Figure 7, the bold curve in Figure 8 is based on the peak frequencies and thin curves show the results from the Monte Carlo simulation. The value $\tau = 0$, about which the solution for ρ is symmetric (in τ), occurs at about MLAT = −2°. The bold curve based on the peak frequencies has a slight "dimple" in ρ at MLAT near −2°; that is, ρ has a local minimum confined to about ±10° from MLAT = −2°. However, the dip in ρ is not great, and the log average solution based on the Monte Carlo simulation does not show such a minimum, indicating that it is probably not statistically significant. Figure 8 shows that the solution based on the peak frequencies and the majority of solutions from the Monte Carlo simulation have a higher value of ρ within about 15° from the magnetic equator than they do at about 25° from the magnetic equator; that is, there is a local maximum in ρ near the magnetic equator.

[30] For most of the solutions, the mass density also starts to increase at large latitude; that is, the mass density decreases as one moves away from the magnetic equator but then increases again at larger latitude. This is consistent with the fact that the mass density must eventually increase at ionospheric latitudes. On the other hand, there is a great

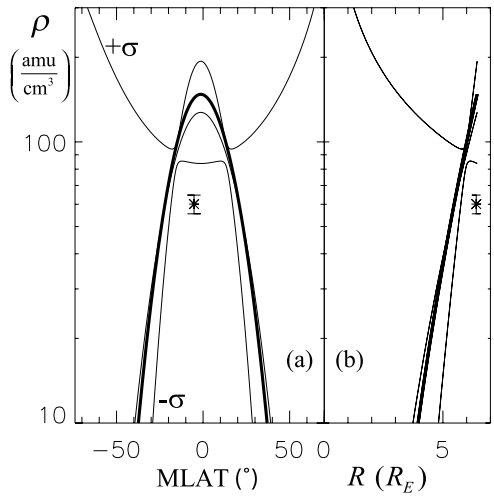

Figure 7. Solutions for mass density ρ as a function of (a) MLAT and (b) R in R_E using the power law form in equation (1). The bold curve is the solution based on the peak frequencies. The middle thin curve is the log average solution based on a Monte Carlo distribution of frequencies using the measured errors in frequency. The upper and lower thin curves are the log average solution plus or minus one standard deviation. The asterisk with error bars is plotted at the numerical value of the observed mass density in amu/cm^{-3} based mainly on data from the Plasma Wave Experiment (PWE).

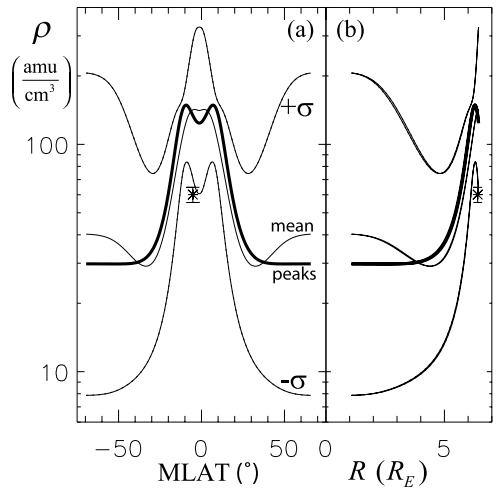

Figure 8. The same as was plotted in Figure 7, except that the polynomial form in equation (2) has been used with coefficients c_0, c_2, c_4, and c_6.

amount of uncertainty in the mass density distribution at large latitude (as indicated by the large separation between the upper and lower thin curves). This can be easily understood based on the WKB formula for the Alfvén frequency $1/f \approx \int dl_s/V_A$; the high-latitude region is where B and hence V_A is large, and it does not have a great affect on the values of the frequencies. Thus when finding the mass density from the frequencies, small changes in the frequencies lead to large variations in ρ at high latitude.

[31] The field line dependence shown in Figure 8 can also be related to the coefficients c_i listed in Table 2. The coefficients based on the Monte Carlo simulation are $c_0 = 2.2 \pm 0.4$, $c_2 = 1.3 \pm 1.4$, $c_4 = -4.9 \pm 2.6$, and $c_6 = 3.1 \pm 2.1$. While it is difficult to make an exact comparison with Figure 8 (without numerically integrating to define the coordinate τ), it is clear that c_2 yields the variation in ρ closest to the magnetic equator (the "dimple") where τ is the smallest, c_4 yields the large drop in ρ between about 10 and 30°, and c_6 (in combination with the other coefficients) leads to an increase in ρ at large MLAT (and τ).

[32] As seen in Figure 7 and 8 or from the observed and theoretical values for ρ_{sc} listed in Table 2, the value of $\rho_{sc,obs}$ (asterisk with error bars in Figures 7 and 8) appears to be a factor of 2–3 below the theoretical mass density at the same latitude based on the toroidal Alfvén frequencies, implying that there may be cold heavy ions present (probably oxygen) consistent with earlier studies [*Waters et al.*, 1996; *Loto'aniu et al.*, 1999; *Chi et al.*, 2000b; *Denton et al.*, 2001]. (Comparing $\rho_{sc,obs}$ with the lower limit of $\rho_{sc,\alpha\text{-ensem}}$ or $\rho_{sc,poly\text{-}ensem}$, the difference is less.) A factor of two increase in mass density requires about a 7% density of oxygen.

4.2. Field Eigenmodes

[33] Each time we solve for the mass density consistent with a set of observed frequencies, we find at the same time the eigenmodes of the toroidal Alfvén harmonics. Figure 9 shows the eigenmodes for the first seven harmonics ($n = 1$–7, where $n = 1$ corresponds to the fundamental) consistent with a solution for ρ using constant density along the field line ($\alpha = 0$ or the polynomial solution with only c_0 nonzero). In the left column are the eigenmodes for δE_x and in the right column are the eigenmodes for δB_y. The wave power is proportional to the square of the field value. Clearly, there are some values of MLAT for which the theoretical solution is large (antinodes), and some values where the theoretical solution is small (nodes).

[34] Since CRRES traverses different MLAT values (Figure 4b), it is possible for us to compare the theoretical prediction about the MLAT distribution of wave power with the range of MLAT values for which the wave power is observed. Figure 10 shows the MLAT distribution of the power spectrum of the observed waves in the frequency range of each harmonic. (The range of MLAT is −8 to −2°, and as can be seen from Figure 4b, this roughly corresponds to 1800–2200 UT.) For instance, for $n = 1$, $f_{obs\text{-}1} = 1.98 \pm 0.45$ mHz (Table 1) and in the bottom two panels of Figure 10 ($n = 1$), the electric field power spectrum (multiplied by frequency) $|\omega\delta E_x|^2$ and the magnetic field power spectrum $|\omega\delta B_y|^2$ are averaged over this frequency range and plotted versus MLAT on the left and right, respectively. Since in each frequency range, the frequency does not vary greatly, we can compare the regions in MLAT where $|\omega\delta E_x|^2$ or $|\omega\delta B_y|^2$ is large with the regions of large amplitude in the theoretical solutions (Figure 9) (that is, since we are comparing the MLAT distribution in a narrow range of frequency, it does not matter that the observed power spectra are multiplied by ω^2). The dashed horizontal lines in each panel show the ranges of MLAT where the power spectrum is large. A band of gray color in a particular panel indicates that the power

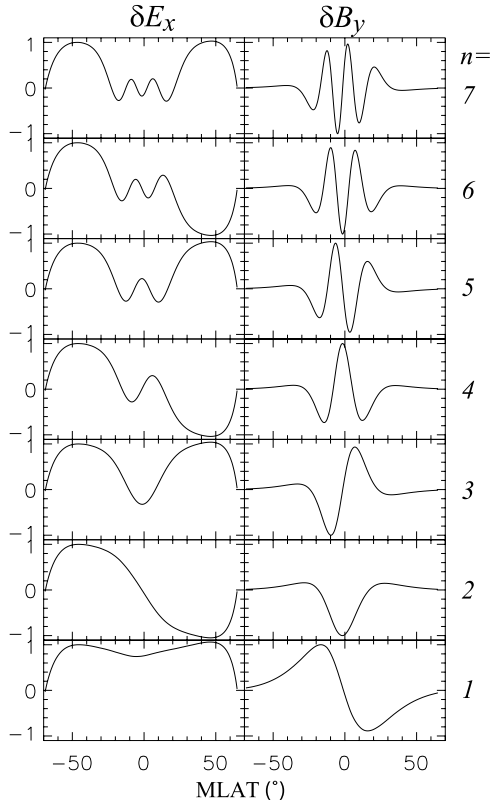

Figure 9. Theoretical eigenmode solutions based on the constant ρ solution ($\alpha = 0$ or "0" polynomial solution) versus MLAT from the southern ionosphere to the northern ionosphere for δE_x (left) and δB_y (right) for the fundamental ($n = 1$ at bottom) to the seventh harmonic ($n = 7$ at top).

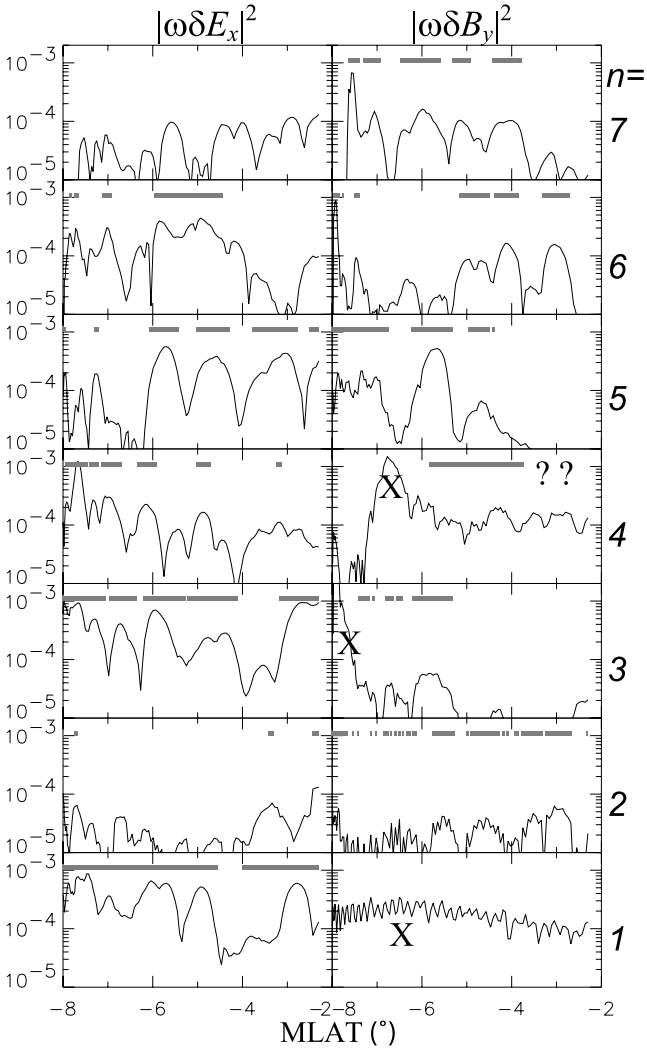

Figure 10. The solid curve in each panel is the observed power spectrum versus MLAT for $|\omega\delta E_x|^2$ in $(\text{mV/(m-s)})^2$ (left) and $|\omega\delta B_y|^2$ in $10^{-2}(\text{nT/s})^2$ (right) averaged in the frequency range for each harmonic (given in Table 1) for the fundamental ($n = 1$ at bottom) to the seventh harmonic ($n = 7$ at top). The gray horizontal segments in each panel show the range where the power spectrum is the largest (as described in the text). The spectral features marked by a cross are spurious (due to noise), and the region marked by question marks is obscured by noise.

spectrum at that range of MLAT lies above the dashed lines in Figure 6 (upper dashed line for the magnetic field power spectrum and lower dashed line for the electric field power spectrum). (Note that these dashed lines have a positive slope to account for the general trend of increasing power at higher frequency because of the whitening of the power spectrum.) For the higher harmonics ($n \geq 4$), note (as in Figure 4) the alternation between the harmonics with odd n, for which there is power in $|\omega\delta E_x|^2$ in the vicinity of the magnetic equator (MLAT $\approx -2°$ at the right side of each panel), and harmonics with even n, for which there is power in $|\omega\delta B_y|^2$ in the vicinity of the magnetic equator.

[35] Figure 11 shows the same eigenmode solutions as were plotted in Figure 9 (solutions for constant ρ), except that the MLAT range plotted is -8 to $-2°$; the horizontal grey bands are the same as were plotted in Figure 10 (showing the latitudinal range of the observed waves). There is a remarkable agreement between the MLAT values where the eigenmodes solutions are largest and the regions where the waves are observed (as indicated by the horizontal grey bands).

[36] The comparison between the MLAT range of observed and theoretical waves in Figure 11 is a powerful demonstration that the harmonics have been identified correctly, and this technique can be used to help identify harmonics. In principle, such a comparison can also help us determine the field line dependence of the mass density, since the eigenmode solutions will not be exactly the same if a different mass density dependence is assumed. However, the variation of the eigenmode solution with respect to the field line distribution is not great. Further work will have to be done to see if this technique can help determine the field line distribution of ρ.

5. Discussion

[37] We have examined in detail electric and magnetic field data measured by the CRRES spacecraft on 29 July 1991 in order to identify toroidal Alfvén waves. Several lines of evidence indicate that we are in fact observing these waves. First of all, the wave emission occurs in discrete bands which have the appearance of harmonics (Figures 2–4). Second, the frequency of these emission bands varies with L shell like

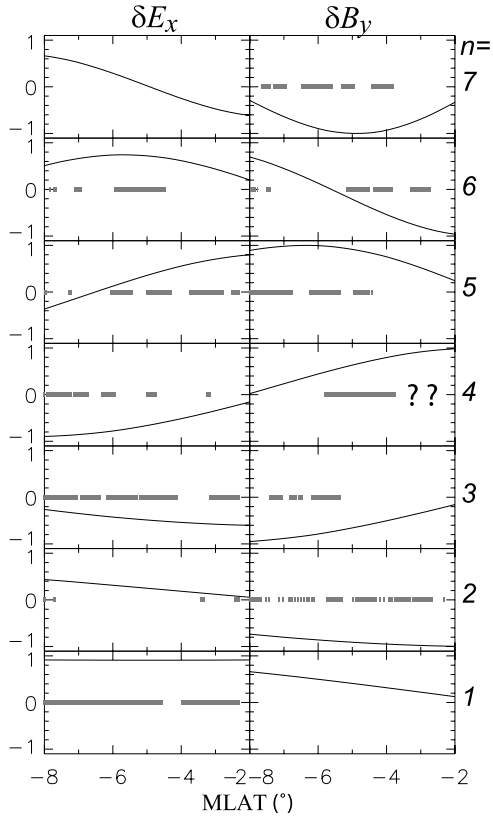

Figure 11. The solid curves in each panel are the same as were plotted in Figure 9, except that the MLAT range plotted is -8 to $-2°$; the gray horizontal segments are the same as were plotted in Figure 10.

$B_{0eq}/(L\sqrt{N_e})$ (Figures 3 and 4), which is the dependence we would expect for an Alfvén wave (scaling like the wave speed divided by the characteristic length). Finally, there is excellent agreement between the latitudinal dependence of the observed waves and theoretical modes (Figure 11). These facts clearly indicate that the observed banded oscillations (azimuthal direction for the magnetic field and radial direction for the electric field) are in fact due to the toroidal Alfvén wave and also show that we understand some of the basic features of these waves.

[38] Another goal of this research was to compute the field line dependence of mass density. While there is a significant uncertainty in the results due to the uncertainty in the observed frequencies, it is nevertheless true that both the solution based on the peak (mean) frequencies and the majority of solutions using a Monte Carlo simulation of the effects of uncertainty in frequency show the same result, that there is a local maximum in ρ within about 30° of the magnetic equator (Figures 7 and 8). The value of ρ may also increase again as MLAT becomes large (Figure 8), as we would expect considering that the densities must increase as ionospheric altitudes are approached. However, our results are very uncertain at high latitudes (Figure 8), owing to the large Alfvén speed there.

[39] It is important to keep in mind that there are a number of assumptions that go into our calculations. We assume that equation (C1) (based on MHD with axisymmetry) describes the waves, that the ionospheric boundary is perfectly conducting, and that equation (2) (which assumes that the mass density distribution is symmetric about the magnetic equator) is adequate to describe the field line distribution (see section 3 and Appendix C).

[40] One important change from our earlier method for calculating the field line dependence of the mass density [*Denton et al.*, 2001] is that we determined the observed frequencies and their uncertainties by averaging the power spectra over a period of time including a number of time windows. This procedure results in an average power spectrum that is more characteristic of the entire wave event than one would find by using the power spectrum from a single time window. We also limited the frequencies to those that were apparent in two-dimensional spectrograms such as Figures 2–4. Using the new method for determining the frequencies, we reexamined the two wave events considered by *Denton et al.* [2001], CRRES orbits 0081 and 0920. In the case of orbit 0920, only three frequencies could be clearly identified using the new method (compared with four used by Denton et al.), and the uncertainties of these were such that the field line distribution was very uncertain. (Also, as mentioned by Denton et al., the second harmonic mode had dominant poloidal, or radial, polarization for the velocity and magnetic fluctuations.) On the other hand, for CRRES orbit 0081 (28 August 1990), eight harmonics could again be clearly identified. Seven of these are listed in Table 1, along with the spacecraft position and other relevant parameters. (Though a peak was apparent for the eighth harmonic, it was at such a high frequency that the power was falling off sharply with respect to frequency and led to some doubt as to the exact location of the peak.)

[41] Figure 12 shows the results of our analysis for the 28 August 1990 event using the polynomial form for the mass density in equation (2). As was the case for Figures 7 and 8, the bold curve is the solution based on the peak frequencies, and the three thin curves are the log average and the log average plus or minus one standard deviation for ρ calculated at each position from the ensemble of solutions in a Monte Carlo simulation. Figure 12 shows a local maximum in mass density within 15° of the magnetic equator, quite similar to that of Figure 8, and verifying the same result that was found by *Denton et al.* [2001]. A local maximum in density at the equator has also been found recently in a statistical study by *Takahashi et al.* [2004]. Their technique compliments the more detailed procedure used in this study. They used an automated procedure to identify Alfvén frequencies for all CRRES wave events with MLT between 1200 and 1800, using both the electric and magnetic field data. They separated the data into L shell bins, $4 < L \leq 5$, $5 < L \leq 6$, and $6 < L \leq 7$. They then normalized the higher frequencies to the fundamental frequency and identified two peaks from the distribution of normalized frequencies, corresponding to the second and third harmonics. The resulting frequency ratios, f_2/f_1 and f_3/f_1, where f_n is the frequency of the nth harmonic, indicated a roughly constant mass density along field lines for $L = 4–5$, consistent with diffusive equilibrium, but a mass density locally peaked at the magnetic equator for $L = 5–7$.

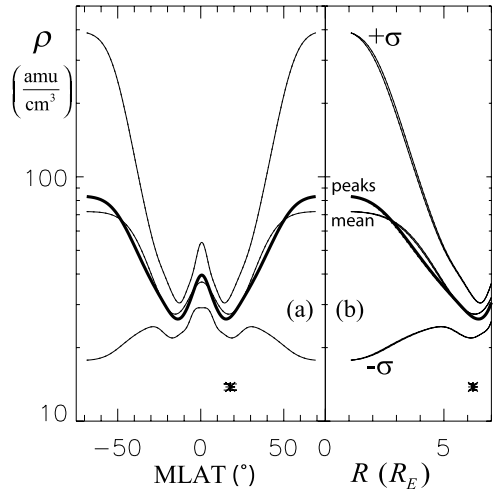

Figure 12. Mass density solutions using the polynomial form in equation (2) as in Figure 8, except based on the toroidal Alfvén frequencies measured on 28 August 1990.

[42] Our two wave events were at $L = 6.4$ (29 July 1991) and 7.2 (28 August 1990), within or beyond Takahashi et al.'s (submitted manuscript, 2004) $L = 6–7$ range. These larger L shell values are usually considered to be in the plasmatrough, where depleted flux tubes may not be in equilibrium. For the 28 August 1990 event, there is some evidence of a plasmapause at about $L = 3.5$ (not shown). However, the 29 July 1991 event does not show clear evidence of a plasmapause (see Figure 2). Also, the density at the time of the 29 July 1991 event is rather high (n_e = 59 cm^{-3}), and the Kp is low (= 1.0 at the time of the event and averaging about 1.5 over the three previous days). Considering these facts, the plasma observed in the 29 July 1991 event could possibly be extended plasmasphere.

[43] While our results, as well as those of *Takahashi et al.* [2004], indicate that the mass density at $L \sim 7$ is locally

peaked at the magnetic equator, such a result has not been found in studies of the field line dependence of the electron density [*Goldstein et al.*, 2001; *Reinisch et al.*, 2001, 2004; *Denton et al.*, 2002a, 2002b]. Taken together, these results may imply that at this distance, heavy ions are preferentially concentrated at the magnetic equator.

Appendix A: LOMICS Mass Density Measurement

[44] In order to compute the observed mass density, we assume that the ions unaccounted for by the LOMICS ion observations are all protons. That is, the observed mass density is given by

$$\rho_{\text{sc,obs}} = \rho_{\text{sc,LOMICS}} + \left(N_{\text{e-sc,obs}} - N_{\text{e-sc,LOMICS}}\right) m_p, \qquad \text{(A1)}$$

where $\rho_{\text{sc,obs}}$ is the observed mass density at the spacecraft location, $\rho_{\text{sc,LOMICS}}$ is the mass density directly observed by LOMICS, $N_{\text{e-sc,obs}}$ is the electron density as determined from PWE, $N_{\text{e-sc,LOMICS}}$ is the electron density for electrons balancing the positive charge of the ions measured by LOMICS, and m_p is the mass of a proton. The value $\rho_{\text{sc,obs}}$ is then a lower limit on the mass density, since there may be cold heavy ions not observed by LOMICS.

Appendix B: Estimation of Uncertainty for Observed Frequencies

[45] In Figure 6, we have the power spectrum in a number of frequency bins. We first find the peaks by searching for local maxima within regions of plus or minus 2 mHz. From the peak, we move outward bin by bin to calculate the standard deviation in frequency. The sums required (sum of linear and squared frequencies) are weighted by the power spectrum in each bin. The sum in each direction is truncated if the power spectrum decreases by a factor of 9 from the peak value or if the power spectrum decreases by a factor of 3 and then starts to increase (the assumption in the latter case is that another peak has been encountered). The peak frequency is calculated from the average frequency obtained in the same way if the peak is sharp and well separated from other peaks; otherwise, a quadratic fit is used of the three power spectrum values around the peak value. In cases for which a peak is measured for both electric and magnetic field data, the two values for frequency are averaged (weighting the individual values with the inverse of the squared uncertainty), yielding a more accurate value for frequency with a smaller standard deviation.

Appendix C: Details Concerning the Calculations

[46] The wave equation (equation (9) of *Singer et al.* [1981], with a misprint in their equation corrected; equation (4) of *Denton et al.* [2001] is also incorrect) is

$$\frac{\partial^2}{\partial s^2}\xi' + \frac{1}{h_\alpha^2 B_0}\frac{\partial}{\partial s}\left(h_\alpha^2 B_0\right)\frac{\partial}{\partial s}\xi' + \frac{\omega^2}{V_A^2}\xi' = 0 \qquad \text{(C1)}$$

where ξ' is the linear displacement in the direction of the oscillation $\hat{\boldsymbol{\alpha}}$ (assumed to be in the azimuthal direction at the magnetic equator) divided by the scale factor h_α (proportional to the displacement to an adjacent field line in the direction of oscillation), $\boldsymbol{B}_0$ is the equilibrium magnetic field, and s is distance along the field line. Equation (C1) requires a magnetic field model as an input; we use the Tsyganenko 96 model [*Tsyganenko*, 1995] if solar wind data is available (28 August 1990) or the Tsyganenko 89 model [*Tsyganenko*, 1989] if the solar wind data is not available (29 July 1991). We adjust the model field along the field line by multiplying by $B_{\text{sc,obs}}/B_{\text{sc,Tsyg}}$ in order to more accurately model the magnitude of the field. (This is a 5% adjustment for 29 July 1991 and a 9% adjustment for 28 August 1990.)

[47] The electric field perturbation is $\delta E_B = i\omega h_\alpha B_0\, \xi'/c$, while the magnetic field perturbation is $\delta B_\alpha = h_\alpha B_0\, (\partial\xi'/\partial s)$ (where $\hat{\boldsymbol{\beta}} = \hat{\boldsymbol{b}}_0 \times \hat{\boldsymbol{\alpha}}$). The ionospheric boundary is placed at a geocentric radius of 1.08 $\boldsymbol{R}_E$ (corresponding to an altitude of 500 km). We will assume that the ionospheric boundary is perfectly conducting (the assumption of *Denton et al.* [2001]), in which case ξ' can be assumed to be real and the boundary condition at the ionospheric boundaries is $\xi' = 0$, corresponding to $\delta E_\beta = 0$.

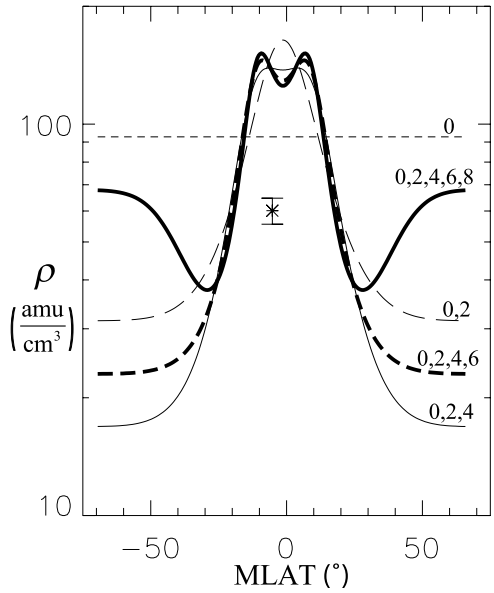

Figure D1. Solutions for mass density ρ as a function of MLAT using even polynomial functions of τ. The set of numerals marking the curves indicates the powers of τ included in the functional dependence of ρ; for instance, the curve marked "0, 2" has a constant term and a term proportional to τ^2. The asterisk with error bars is plotted at a value of mass density based mainly on data from PWE.

Appendix D: Solutions Using Different Sets of Polynomial Coefficients

[48] In section 4, we described mass density solutions using a polynomial expansion (equation (2)) in the Alfvén crossing time τ (equation (3)) with four nonzero coefficients, c_0, c_2, c_4, and c_6. In this appendix, we explore how the solution changes if we use different sets of coefficients c_i. In each case, we vary the coefficients c_i so that the deviation between the theoretical and observed frequencies σ_f defined in equation (4) is minimized. Again, we use only

Table D1. Values of the Frequency Deviation Parameter σ_f for Wave Event on 29 July 1991 for Different Numbers of Polynomial Coefficients N_p

N_p	Polynomial Coefficients	σ_f
1	c_0	0.061
2	c_0, c_2	0.024
3	c_0, c_2, c_4	0.014
4	c_0, c_2, c_4, c_6	0.010
5	c_0, c_2, c_4, c_6, c_8	0.005

even powers of τ in equation (3) so that the mass density distribution is symmetric with respect to τ (and approximately symmetric with respect to the distance along the field line from the magnetic equator s).

[49] Figure D1 shows the results for the mass density ρ as a function of MLAT. The labels next to the curves indicate the set of polynomial coefficients used. That is, the curve marked "0" represents the solution with only c_0 nonzero so that the mass density is constant along the field line, the curve marked "0, 2" represents the solution using a quadratic form $\log_{10} \rho = c_0 + c_2\tau^2$ the curve marked "0, 2, 4" represents the solution with c_0, c_2, and c_4 nonzero, etc. The solutions with a large number of coefficients are not necessarily unique (there may be more than one solution that minimizes σ_f); we show the solution with the lowest σ_f that we found. Our procedure for minimizing σ_f includes a grid search in the parameters c_i to find the minimum σ_f; however, this search is necessarily limited to keep the computational time manageable. Our solution with six coefficients ("0, 2, 4, 6, 8, 10") was not significantly different from the solution for five coefficients.

[50] The value $\tau = 0$, about which the solution for ρ is symmetric (in τ), occurs at about MLAT = $-2°$. Starting with the curve labeled "0, 2, 4," there is a slight "dimple" in ρ at MLAT near $-2°$; that is, ρ has a local minimum confined to about $\pm 10°$ from MLAT = $-2°$. This feature is probably not statistically significant (see the discussion in section 4.1). Aside from the "0" curve (constant ρ), all the solutions show that ρ is decreasing with respect to distance away from the magnetic equator at MLAT ~ 15–$20°$. Beyond about $30°$ from the magnetic equator, the solutions differ. The "0, 2, 4, 6, 8" solution indicates that ρ increases at large latitudes. This result is what we would expect considering that at some large latitude, the density should start to increase toward ionospheric values. On the other hand, this high latitude region is also where the Monte Carlo technique leads to large uncertainty (Figure 8). The values of σ_f for each solution are listed in Table D1.

[51] **Acknowledgments.** We acknowledge helpful conversations with Dieter Bilitza, Casandra Fesen, Arthur Richmond, David Southwood, and Eugene Demidenko. We thank Jeffrey Hughes for supplying CRRES electric and magnetic field data. This work was supported by NASA grants NAG5-11825, NAG5-12201, and NAG 5-11735.

[52] Arthur Richmond thanks Peter Chi and Mark B. Moldwin for their assistance in evaluating this paper.

References

Anderson, B. J., M. J. Engebretson, S. P. Rounds, L. J. Zanetti, and T. A. Potemra (1990), A statistical study of Pc 3–5 pulsations observed by the AMPTE CCE magnetic fields experiment: 1. Occurrence distributions, *J. Geophys. Res.*, *95*(A7), 10,495–10,523.

Anderson, R. R., D. A. Gurnett, and D. L. Odem (1992), CRRES Plasma Wave experiment, *J. Spacecr. Rockets*, *29*(4), 570–573.

Chi, P. J., C. T. Russell, S. Musman, W. K. Peterson, G. Le, V. Angelopoulos, G. D. Reeves, M. B. Moldwin, and F. K. Chun (2000a), Plasmaspheric depletion and refilling associated with the September 25, 1998 magnetic storm observed by ground magnetometers at L = 2, *Geophys. Res. Lett.*, *27*(5), 633–636.

Chi, P. J., C. T. Russell, M. F. Thomsen, W. K. Peterson, and S. M. Petrinec (2000b), Multi-point observations of the magnetospheric plasma density during the September 1998 magnetic storm, *EOS Trans. AGU*, *81*(48), Fall Meet. Suppl., F1054.

Denton, R. E., and D. L. Gallagher (2000), Determining the mass density along magnetic field lines from toroidal eigenfrequencies, *J. Geophys. Res.*, *105*(A12), 27,717–27,725.

Denton, R. E., M. R. Lessard, R. Anderson, E. G. Miftakhova, and J. W. Hughes (2001), Determining the mass density along magnetic field lines from toroidal eigenfrequencies: Polynomial expansion applied to CRRES data, *J. Geophys. Res.*, *106*(A12), 29,915–29,924.

Denton, R. E., J. Goldstein, J. D. Menietti, and S. L. Young (2002a), Magnetospheric electron density model inferred from Polar plasma wave data, *J. Geophys. Res.*, *107*(A11), 1386, doi:10.1029/2001JA009136.

Denton, R. E., J. Goldstein, and J. D. Menietti (2002b), Field line dependence of magnetospheric electron density, *Geophys. Res. Lett.*, *29*(24), 2205, doi:10.1029/2002GL015963.

Engebretson, M. J., L. J. Zanetti, T. A. Potemra, and M. H. Acuna (1986), Harmonically structured ULF pulsations observed by the AMPTE CCE magnetic field experiment, *Geophys. Res. Lett.*, *13*(9), 905–908.

Goldstein, J., R. E. Denton, M. K. Hudson, E. G. Miftakhova, S. L. Young, J. D. Menietti, and D. L. Gallagher (2001), Latitudinal density dependence of magnetic field lines inferred from polar plasma wave data, *J. Geophys. Res.*, *106*(A4), 6195–6201.

Ledocq, M. J., D. A. Gurnett, and R. R. Anderson (1994), Electron number density fluctuations near the plasmapause observed by the CRRES spacecraft, *J. Geophys. Res.*, *99*(A12), 23,661–23,671.

Lessard, M. R., M. K. Hudson, and H. Luhr (1999), A statistical study of Pc3-Pc5 magnetic pulsations observed by the AMPTE/Ion Release Module satellite, *J. Geophys. Res.*, *104*(A3), 4523–4538.

Loto'aniu, T. M., C. L. Waters, B. J. Fraser, and J. C. Samson (1999), Plasma mass density in the plasmatrough: Comparison using ULF waves and CRRES, *Geophys. Res. Lett.*, *26*(21), 3277–3280.

Maynard, N. C., W. J. Burke, E. M. Basinska, G. M. Erickson, W. J. Hughes, H. J. Singer, A. G. Yahnin, D. A. Hardy, and F. S. Mozer (1996), Dynamics of the inner magnetosphere near times of substorm onsets, *J. Geophys. Res.*, *101*(A4), 7705–7736.

Menk, F. W., D. Orr, M. A. Clilverd, A. J. Smith, C. L. Waters, D. K. Milling, and B. J. Fraser (1999), Monitoring spatial and temporal variations in the dayside plasmasphere using geomagnetic field line resonances, *J. Geophys. Res.*, *104*(A9), 19,955–19,969.

Price, I. A., C. L. Waters, F. W. Menk, G. J. Bailey, and B. J. Fraser (1999), A technique to investigate plasma mass density in the topside ionosphere using ULF waves, *J. Geophys. Res.*, *104*(A6), 12,723–12,732.

Reinisch, B. W., X. Huang, P. Song, G. S. Sales, S. F. Fung, J. L. Green, D. L. Gallagher, and V. M. Vasyliunas (2001), Plasma density distribution along the magnetospheric field: RPI observations from IMAGE, *Geophys. Res. Lett.*, *28*(24), 4521–4524.

Reinisch, B. W., X. Huang, P. Song, J. L. Green, S. F. Fung, V. M. Vasyliunas, D. L. Gallagher, and B. R. Sandel (2004), Plasmaspheric mass loss and refilling as a result of a magnetic storm, *J. Geophys. Res.*, *109*, A01202, doi:10.1029/2003JA009948.

Singer, H. J., and M. G. Kivelson (1979), The latitudinal structure of Pc 5 waves in space: Magnetic and electric field observations, *J. Geophys. Res.*, *84*, 7213–7222.

Singer, H. J., C. T. Russell, M. G. Kivelson, T. A. Fritz, and W. Lennartsson (1979), Satellite observations of the spatial extent and structure of Pc 3,4,5 pulsations near the magnetospheric equator, *Geophys. Res. Lett.*, *6*(11), 889–892.

Singer, H. J., D. J. Southwood, R. J. Walker, and M. G. Kivelson (1981), Alfven wave resonances in a realistic magnetospheric magnetic-field geometry, *J. Geophys. Res.*, *86*(A6), 4589–4596.

Singer, H. J., W. P. Sullivan, P. Anderson, F. Mozer, P. Harvey, J. Wygant, and W. McNeil (1992), Fluxgate magnetometer instrument on the CRRES, *J. Spacecr. Rockets*, *29*(4), 599–601.

Takahashi, K., and R. L. McPherron (1982), Harmonic structure of Pc 3–4 pulsations, *J. Geophys. Res.*, *87*(A3), 1504–1516.

Takahashi, K., et al. (2004), Frequencies of standing Alfvén wave harmonics and their implication for plasma mass distribution along geomagnetic field lines: Statistical analysis of CRRES data, *J. Geophys. Res.*, *109*, doi:10.1029/2003JA010345, in press.

Tsyganenko, N. A. (1989), A magnetospheric magnetic field model with a warped tail current sheet, *Planet. Space Sci.*, *37*, 5–20.

Tsyganenko, N. A. (1995), Modeling the Earth's magnetospheric magnetic field confined within a realistic magnetopause, *J. Geophys. Res.*, *100*(A4), 5599–5612.

Waters, C. L., J. C. Samson, and E. F. Donovan (1996), Variation of plasmatrough density derived from magnetospheric field line resonances, *J. Geophys. Res.*, *101*(A11), 24,737–24,745.

Wygant, J. R., P. R. Harvey, D. Pankow, F. S. Mozer, N. Maynard, H. Singer, M. Smiddy, W. Sullivan, and P. Anderson (1992), CRRES electric field Langmuir probe instrument, *J. Spacecr. Rockets*, *29*(4), 601–604.

Young, D. T., B. L. Barraclough, D. J. McComas, M. F. Thomsen, K. McCabe, and R. Vigil (1992), CRRES low-energy magnetospheric ion composition sensor, *J. Spacecr. Rockets*, *29*(4), 596–598.

R. R. Anderson, Department of Physics and Astronomy, 615 Van Allen Hall, University of Iowa, Iowa City, IA 52242, USA. (rra@space.physics.uiowa.edu)

R. E. Denton, Department of Physics and Astronomy, 6127 Wilder Laboratory, Dartmouth College, Hanover, NH 03755, USA. (richard.denton@dartmouth.edu)

K. Takahashi, Applied Physics Laboratory, Johns Hopkins University, 11100 Johns Hopkins Road, Laurel, MD 20723, USA. (kazue.takahashi@jhuapl.edu)

M. P. Wuest, INFICON Limited, Alte Landstrasse 6, FL-9496 Balzers, Principality of Liechtenstein. (martin.wuest@inficon.com)